

Highlights from the CALET observations for 7.5 years on the International Space Station

Shoji Torii for the CALET collaboration

Waseda University,
17 Kikuicho, Shinjuku, Tokyo, Japan
E-mail: torii.shoji@wasea.jp

The CALorimetric Electron Telescope (CALET) space experiment is a high-energy astroparticle physics mission installed on the International Space Station (ISS). The primary goals of the CALET mission include studying the details of galactic cosmic-ray acceleration and propagation, and searching for possible nearby sources of high-energy electrons and dark matter signatures. The CALET experiment is measuring the flux of cosmic-ray electrons (including positrons) to 20 TeV, gamma-rays to 10 TeV and nuclei with $Z=1$ to 40 up to 1,000 TeV. The instrument consists of two layers of segmented plastic scintillators for the identification of cosmic-rays via a measurement of their charge (CHD), a 3 radiation length thick tungsten-scintillating fiber imaging calorimeter (IMC) and a 27 radiation length thick lead-tungstate calorimeter (TASC). The instrument was launched on August 19, 2015 to the ISS and installed on the Japanese Experiment Module-Exposed Facility (JEM-EF). Since the start of operations in mid-October, 2015, CALET has been in continuous observation mode over 7.5 years and mainly triggering on high energy (>10 GeV) cosmic-ray showers without any major interruption. The number of triggered events over 10 GeV is nearly 1.86 billion events as of June 30, 2023. Here, we present the highlights of the CALET latest results, including the electron + positron energy spectrum, the spectra of protons and other nuclei, gamma-ray observations, as well as the characterization of on-orbit performance. Some results on the electromagnetic counterpart search for LIGO/Virgo gravitational wave events and the observations of solar modulation and gamma-ray bursts are also included.

38th International Cosmic Ray Conference (ICRC2023)
26 July - 3 August, 2023
Nagoya, Japan



1. Introduction

The CALorimetric Electron Telescope (CALET) is a space experiment aboard the ISS, designed for long-term observations of charged and neutral cosmic radiation. The mission is managed by an international collaboration led by the Japanese Space Agency (JAXA) with the participation of the Italian Space Agency (ASI) and the US Space Agency (NASA). It was launched on August 19, 2015 with the Japanese carrier H-IIB, delivered to the ISS by the HTV-5 Transfer Vehicle, and installed on the Japanese Experiment Module Exposure Facility (JEM-EF).

The science program of CALET addresses several outstanding questions of high-energy astroparticle physics including the origin of cosmic rays (CR), the possible presence of nearby astrophysical CR sources, the acceleration and propagation of primary and secondary elements in the galaxy, and the nature of dark matter. The design of CALET is optimized for high precision measurements of the electron+positron (all electron) spectrum with an accurate scan of the energy interval already covered by previous experiments and its extension to the region above 1 TeV. Given the high energy resolution of CALET for electrons, a detailed study of the spectral shape might reveal the presence of nearby sources of acceleration as well as possible indirect signatures of dark matter. With its capability of identifying CRs with individual element resolution, CALET is also carrying out direct measurements of the spectra and relative abundances of light and heavy cosmic nuclei, from proton to nickel, in the energy interval from 50 GeV (for the lighter nuclei, 10 GeV/ n for the heavier) to several hundred TeV. The abundances of trans-iron elements up to $Z=40$ are studied with a dedicated program of long term observations.

In addition to the charged CRs, the observation of high energy gamma-ray from 1 GeV to 10 TeV is carried out in conjunction with the CALET Gamma-ray Burst Monitor (CGBM) which covers from the hard X-ray to the soft Gamma-ray region (7 keV–20 MeV). CALET contributes also on observations for the solar modulation of electrons and protons in 1–10 GV, and on detection of the MeV electrons from the radiation belt (relativistic electron precipitation: REP) for space weather. Figure 1 shows overview of the CALET payload and CALET emplaced on the No. 9 port of JEM-EF.

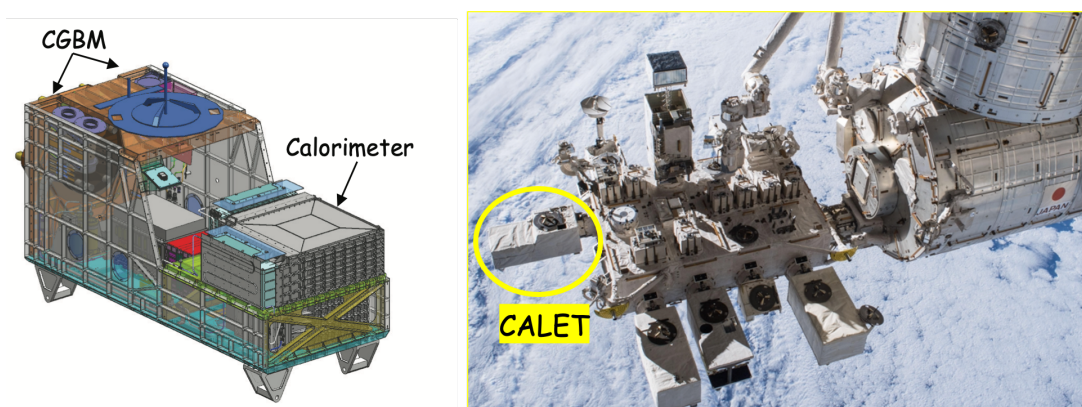


Figure 1: Overview of CALET payload (left) and CALET emplaced on the JEM-EF (right).

2. The CALET Instrument

The CALET calorimeter (see Fig. 2) consists of a charge detector (CHD), which identifies the charge of the incident particle, an imaging calorimeter (IMC), which reconstructs the track of the incident particle and records the initial shower development with fine resolution, and a total absorption calorimeter (TASC), which absorbs the energy of the electromagnetic shower particles and identifies the particle species using hodoscopic lead-tungstate crystal arrays.

Plastic scintillators arranged in two orthogonal layers, each containing 14 scintillator paddles ($3.2 \times 1.0 \times 45.0 \text{ cm}^3$), constitute the CHD. These paddles generate photons that are detected by a photomultiplier tube (PMT), and the resulting output is sent to a front-end circuit (FEC). This FEC and the readout system that follows it have sufficient dynamic range for detecting particle charges in the range of $Z=1-40$. The initial shower is resolved by the sampling calorimeter of the IMC, which was carefully designed to accurately determine the shower starting point and incident direction. The IMC contains a total of 16 detection layers, arranged in 8 X-Y pairs, with each layer segmented into 448 parallel scintillating fibers ($0.1 \times 0.1 \times 44.8 \text{ cm}^3$), which are individually read out by 64-channel multi-anode PMTs. Tungsten plates are placed between X-Y pairs. The total thickness of tungsten is $3 X_0$: five upper layers of tungsten plates each with $0.2 X_0$ thickness and two lower tungsten layers each of thickness $1.0 X_0$. The TASC has an overall depth of $27 X_0$ and consists of 12 detection layers in an alternating orthogonal arrangement, each comprising 16 lead-tungstate crystal (PbWO_4 or PWO) logs with dimensions of $2.0 \times 1.9 \times 32.6 \text{ cm}^3$. This design allows the TASC to image the development of a shower in three dimensions. With the exception of the first layer, which uses PMTs, a photodiode (PD) in conjunction with an avalanche photodiode (APD) reads the photons generated by each PWO log. Two shaping amplifiers with different gains for each APD (PMT) and PD are used to achieve a dynamic range of 10^6 (10^4).

With these sub-detectors, the trigger system and the data acquisition system, the CALET instrument has a proton rejection factor of larger than 10^5 , a 2% energy resolution above 20 GeV for electrons, a very wide dynamic range from 1 GeV to 1 PeV, a charge resolution of 0.1–0.3 electron charge units from protons to above iron (up to $Z=40$), an angular resolution of 0.1 to 0.5° , and a geometrical factor on the order of $0.1 \text{ m}^2 \text{ sr}$. Figure 3 shows an observed electron candidate with energy 3.05 TeV. The instrument is described in more detail elsewhere [1, 2].

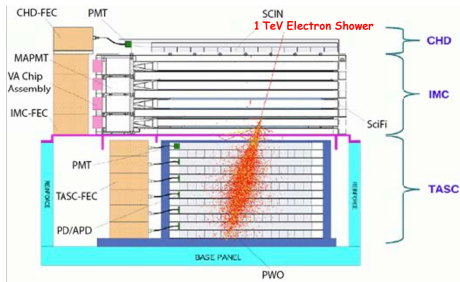


Figure 2: Schematic side view of CALET in which simulated 1 TeV electron is over-written.

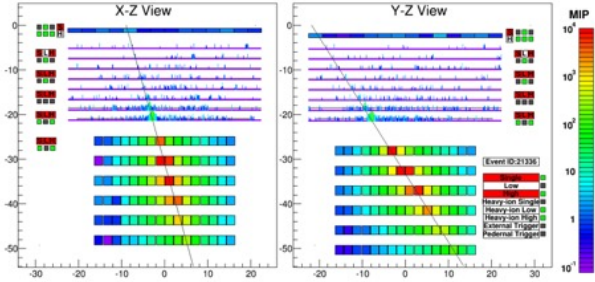


Figure 3: Example of observed electron candidate with an energy of 3.05 TeV in XZ-YZ view.

3. Orbital Operations and Calibrations

The on-orbit operation of CALET, described in Ref. [3], have remained very stable due to the excellent collaboration between JAXA Ground Support Equipment (JAXA-GSE) and the Waseda CALET Operations Center (WCOC) [4]. A continuously active high-energy (HE: $E > 10 \text{ GeV}$) trigger mode ensures maximum exposure to high-energy electrons and other high-energy shower events. The other modes include a low-energy electron trigger in high-geomagnetic latitudes, a low-energy gamma-ray ($\text{LE-}\gamma$) trigger in low-geomagnetic latitudes, and an almost continuously active ultra-heavy trigger mode, during each ISS orbit. The total observation time was 2818 days as of June 30, 2023. The live-time fraction was $\sim 86\%$ for this period. More than 1.68 billion events were observed in HE trigger mode.

One important feature of CALET and other thick calorimeter instruments is their excellent energy resolution in the TeV region. However, calibration errors must still be carefully evaluated and considered when estimating the energy resolution. Our energy calibration includes

an evaluation of conversion factors between ADC units and energy deposits, confirming linearity over each of the gain ranges (TASC has four gain ranges for each channel), as well as a seamless transition between adjacent gain ranges. Temporal gain variations that occur during long-term observations are also corrected in the calibration [2]. We have estimated the errors at each calibration step, such as the correction of position and temperature dependence, linear fit procedure of each gain range, gain ratio measurements, and slope extrapolation, as well as the errors inferred from the degree of consistency between energy deposit peaks of non-interacting protons and helium. These errors are included in the estimation of the energy resolution. This results in a very high resolution of 2% or better above 20 GeV [2].

It's worth noting that, even though this calibration is extensive, its uncertainty is a limiting factor for the energy resolution. The intrinsic resolution (i.e., design capability) of CALET is 1%. In addition, the calibration error in the lower gain ranges are crucial for spectrum measurements in the TeV range. The TASC energy deposit spectrum based on all triggered events through the end of June 2023 is shown in Fig. 4. The first and second bumps are due to low- and high-energy triggered events, respectively, whereas the high-energy tail is due to the power-law nature of the cosmic-ray spectrum. This spectrum spans more than six orders of magnitude in energy, from below 1 GeV to above 1 PeV. This clearly demonstrates the reliability of CALET energy measurements over a very wide dynamic range.

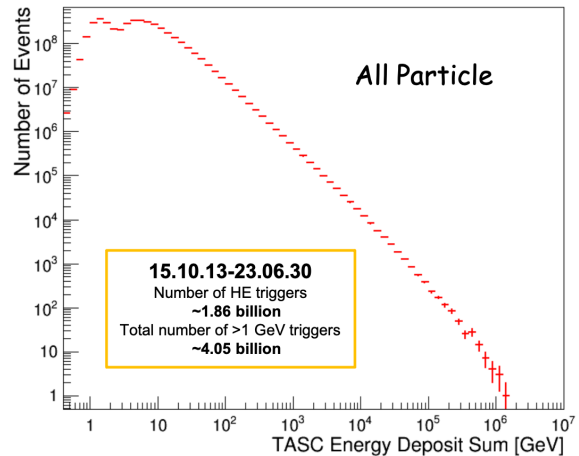


Figure 4: TASC energy-deposit spectrum observed from 1 GeV to above 1 PeV (see text).

4. Results

4.1 Precise Measurement of the Electron+Positron Spectrum

The new results of the electron + positron (all-electron) spectrum with CALET are presented at this conference [5] and will be published soon [6], based on 2637 days of flight data collected with the high-energy shower trigger. The flux shown in Fig. 5 corresponds to an increase by a factor of 3.4 of the available statistics with respect to the last CALET all-electron spectrum publication [7]. The spectrum integrates 7.02 million electron (+ positron) events above 10.6 GeV up to 7.5 TeV. The error bars along the horizontal and vertical axes are representative of the bin width and statistical errors, respectively. The gray band bounds the quadrature sum of statistical and systematic errors. The CALET design is optimized for the precise measurement of the all-electron spectrum from 10 GeV to 20 TeV with a field of view of 45 degrees from the zenith and a geometrical factor of $1040 \text{ cm}^2 \text{ sr}$ at high energies [1]. The $30 X_0$ -thick calorimeter allows for a full containment of electron showers even at the TeV scale, with an excellent energy resolution ($< 2\%$ above 20 GeV), while proton showers of equivalent energy deposit undergo a larger energy leakage from the bottom layers of the TASC. This feature is exploited to separate electrons from protons, building upon the capability of the TASC and IMC to image the longitudinal and lateral profiles of electromagnetic and hadronic cascades. Two methods were applied to identify electrons and to study systematic uncertainties in the electron identification: a simple two-parameter cut and a multivariate analysis based on boosted decision trees (BDTs). In the final electron sample, the residual contamination of protons is 5% up to 1 TeV, and less than 10% in the 1–7.5 TeV region, while keeping a constant high

efficiency of 70% for electrons including the pre-selection efficiency. An independent confirmation of the proton rejection power at high energies is discussed in Ref. [8].

Systematic uncertainties include the absolute normalization error as well as energy dependent errors stemming from BDT stability, trigger efficiency in the low-energy region, tracking performance, dependence on charge and electron identification methods, and MC model dependence. Conservatively, all of them are included in the total error estimate of Fig. 5. The absolute energy scale was calibrated and shifted by +3.5% as a result of studies of the geomagnetic cutoff energy. The systematic uncertainties are described in more detail in Ref. [5].

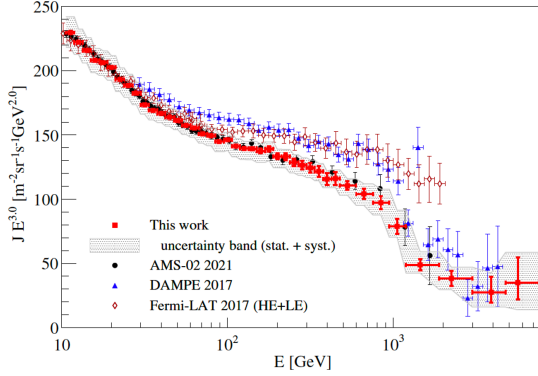


Figure 5: All-electron spectrum observed with CALET, where the gray band indicates the quadratic sum of statistical and systematic errors. Also plotted are other direct measurements in space [9–11].

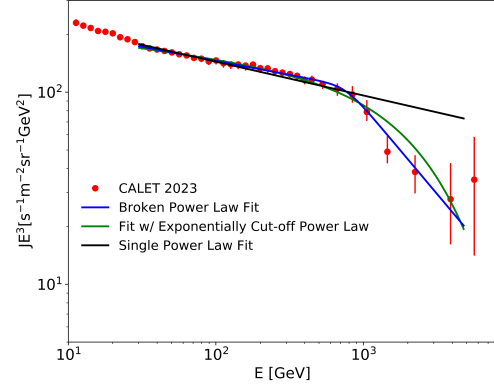


Figure 6: Fitted results of all-electron spectrum in the energy range from 30 GeV to 4.8 TeV, with a broken power law, an exponentially cutoff power law and a single power law.

Comparing with the other space experiments (Fermi-LAT, AMS-02 and DAMPE), the CALET spectrum shows a good agreement with AMS-02 data up to 2 TeV, where both experiments have a good electron identification capability, albeit using different detection techniques. In the energy region from 30 to 300 GeV, the fitted power-law spectrum index, -3.14 ± 0.02 , is roughly consistent with the values quoted by other experiments within the errors. However, the CALET spectrum appears to be softer compared to Fermi-LAT and DAMPE, and the flux measured by CALET is lower than those by Fermi-LAT and DAMPE, starting near 60 GeV and extending to near 1 TeV, possibly indicating the presence of unknown systematic errors.

The electron energy spectrum above 1 TeV is expected to show a break due to the radiative cooling process with an energy loss rate proportional to E^2 . As a result, only nearby (< 1 kpc) and young ($< 10^5$ years) sources can contribute to the flux above 1 TeV if the sources are supernova remnants (SNRs) as it is commonly believed [12, 13]. The expected flux suppression above 1 TeV is clearly seen by CALET and is consistent with DAMPE within errors. As presented in Fig. 6, the spectrum is fitted in the energy range from 30 GeV to 4.8 TeV with a broken power law and an exponentially cutoff power law. The significance of both fits is more than 6.5σ compared to a single-power law fit with index of -3.18 ± 0.01 . Combining the CALET all-electron spectrum and the positron measurements up to 1 TeV by AMS-02, we attempt a consistent interpretation of both spectra based on contributions from pulsars and nearby SNR sources. Details of the interpretation using the all-electron spectrum up to 4.8 TeV [14] and the positron measurement [15] are discussed in Ref. [16]. Based on this interpretation, the obtained spectrum in the TeV region is tested for indications of contributions from the nearby sources, foremost Vela, by estimating the number of electron candidates above 4.8 TeV. However, the electron identification above 4.8 TeV should be carefully checked due to increasing contamination at high energies by background protons. The updated interpretation will be published by using the latest results of the CALET all-

electron spectrum [6], obtained with an event-by-event analysis with a residual proton contamination probability less than 10% up to 20 TeV [17]. Moreover, Dark Matter limits in the mass interval from 100 GeV to several 10 TeV are investigated by modeling the astrophysical background using the both data-sets of all-electron and positron [18].

4.2 Proton and Helium Spectrum

A new proton spectrum with CALET was presented at this conference [19], based on a restricted dataset collected within a fiducial geometrical acceptance ($510 \text{ cm}^2 \text{ sr}$) during 2757 days of operation with the High Energy (HE) trigger and 365.4 hrs of live time with the Low Energy trigger (LE) [20], respectively. It is an update of the published CALET proton spectrum [21] by increasing the statistics by 21%, and the energy range is from 50 GeV to 60 TeV as shown in Fig. 7. In the same figure the CALET flux is compared with AMS-02 [22], CREAM-III [23], and DAMPE [24]. In the low energy region with $E < 200 \text{ GeV}$, the result is fully consistent. In the higher energy region, a systematic difference is observed, but the difference is within the errors. We confirm the presence of a spectral hardening around 500 GeV as reported in Ref. [20]. We also observe a spectral softening around 10 TeV. In order to quantify the spectral hardening and softening, we fit the proton spectrum using a Double Broken Power Law (DBPL) function defined as follows:

$$\Phi(E) = C \left(\frac{E}{1 \text{ GeV}} \right)^\gamma \left[1 + \left(\frac{E}{E_0} \right)^s \right]^{\frac{\Delta\gamma}{s}} \left[1 + \left(\frac{E}{E_1} \right)^{s_1} \right]^{\frac{\Delta\gamma_1}{s_1}} \quad (1)$$

where C is a normalization factor, γ is the spectral index, E_0 is a characteristic energy of the region where a gradual spectral hardening is observed, $\Delta\gamma$ is the spectral variation due to the spectral hardening, E_1 is a characteristic energy of the transition to the region of spectral softening, $\Delta\gamma_1$ is the spectral index variation observed above E_1 . Two independent smoothness parameters S and S_1 are introduced in the energy intervals where spectral hardening and softening occur, respectively. In Fig. 8, the black filled circles show the data with statistical errors and the red line shows the best fitted function for $\Phi'(E) = E^{2.7} \times \Phi(E)$. The χ^2 is 6.0 with 20 degrees of freedom. The best fit parameters are summarized in Table 1.

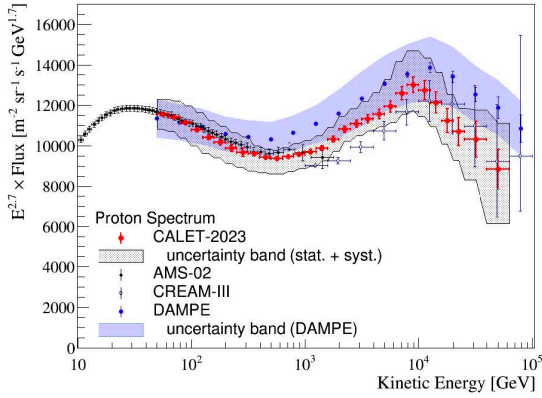


Figure 7: Proton spectrum measured by CALET (red) compared with other experiments (AMS02, CREAM-III, DAMPE). The hatched band shows the total uncertainty for CALET. The dark blue colored band shows the total uncertainty for DAMPE.

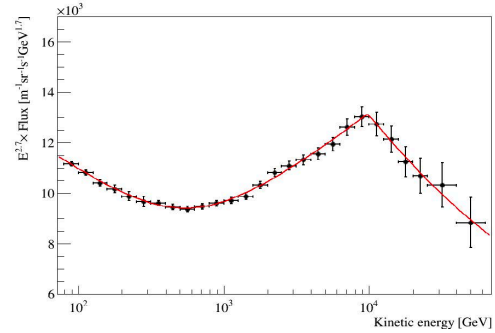


Figure 8: CALET proton spectrum fitted by a DBPL function (Eq. 1: red solid line). The horizontal error bars are representative of the bin width.

The helium spectrum was published in Ref. [25] and reported in this conference [26] as shown in Fig. 9, where it is compared with previous observations from space-based [27, 28] and balloon-

borne [29] experiments. This result was obtained during 2392 days of operations, collected within a restricted "fiducial" geometrical acceptance ($510 \text{ cm}^2 \text{ sr}$) which amounts to about one half of the total acceptance. A study is ongoing to attempt increasing the acceptance by a factor of nearly two by applying a new analysis to consider events entering from the side edges of the IMC [30].

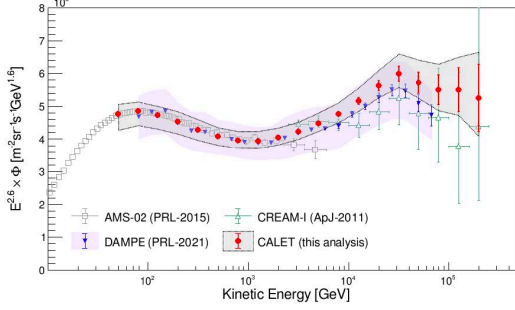


Figure 9: Helium spectrum with CALET (red markers), compared with other observations. The error bars represent only the statistical error. The gray band represents the total uncertainty for CALET; the violet band for DAMPE.

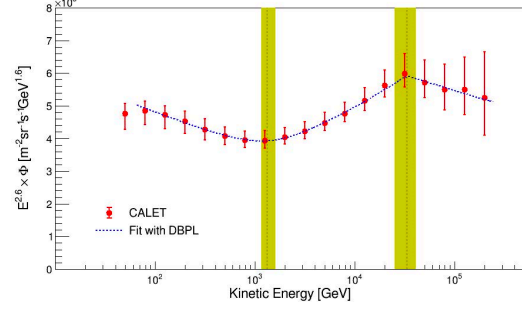


Figure 10: Fit of CALET data with a DBPL function (Eq. 1). Both statistical and systematic uncertainties are taken into account. The yellow bands indicate the energy regions of hardening and softening, respectively (see text).

In Fig. 10, a fit of the helium spectrum has been performed using a DBPL function (as used above), in the energy range from 60 GeV to 250 TeV. A progressive hardening from a few hundred GeV to a few tens TeV and the onset of a flux softening above a few tens of TeV are observed, which are indicated by the yellow bands. The best fit parameters (given only for statistical errors) are summarized in Table 1 to compare with the proton results.

Table 1: Best fit parameters with DBPL function (Eq. 1) for proton and helium spectrum.

	γ	E_0 (GeV)	$\Delta\gamma$	S	E_1 (TeV)	$\Delta\gamma_1$	S_1
Proton	-2.843 ± 0.005	553^{+44}_{-38}	0.29 ± 0.01	2.1 ± 0.4	$9.8^{+3.2}_{-2.1}$	$-0.39^{+0.15}_{-0.18}$	~ 90
Helium	$-2.703^{+0.005}_{-0.006}$	1319^{+113}_{-93}	$0.25^{+0.02}_{-0.01}$	$2.7^{+0.6}_{-0.5}$	$33.2^{+9.8}_{-6.2}$	$-0.22^{+0.07}_{-0.10}$	30

Differences between the proton and helium spectra can contribute important constraints on acceleration models. To ease the comparison in Fig. 11, we show the CALET proton spectrum published in Ref. [21] and the helium spectrum as a function of rigidity (see the SM of Ref. [25]). The ^3He contribution to the flux is taken into account assuming the same $^3\text{He}/^4\text{He}$ ratio as measured by AMS-02 [31] and extrapolating it to higher energies with use of a single power-law fit. Measurements from other experiments [28, 32] are included in these plots. Our result is found to be in agreement with measurements from the magnetic spectrometers up to their maximum detectable rigidity ($\sim 2 \text{ TV}$). The p/He flux ratio measured by CALET is presented in Fig. 12 as a function of rigidity with statistical errors only with the other experiments.

4.3 Heavy Nuclei Flux and These Ratios

Carbon, Oxygen and Boron The spectra of cosmic-ray carbon, oxygen, boron and their ratios were published by CALET in Ref. [33, 34] and presented at this conference by an analysis of the data during 2554 days of CALET operation [35]. The total background contamination of B is 1% for $E_{TASC} < 10^2 \text{ GeV}$ and grows logarithmically with E_{TASC} above 10^2 GeV , approaching 7% at 1.5 TeV. The background contamination is $< 1\%$ in C and O spectra. The isotopic composition of boron is assumed as $^{11}\text{B}/(^{10}\text{B} + ^{11}\text{B}) = 0.7$ for all energies. Different values of the isotope ratio (0.6 and 0.8) make only a 2% difference in the boron spectrum. The spectra are shown in Fig. 13 in an energy range from 8.4 GeV/ n to 3.8 TeV/ n where uncertainties, including statistical

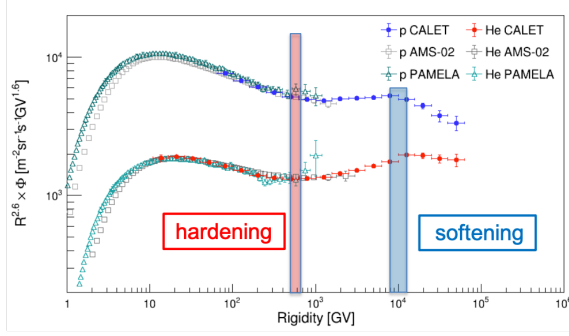


Figure 11: Proton and Helium spectrum with CALET vs. Rigidity. The red and blue bands show the spectral hardening and softening region, respectively. Results from PAMELA and AMS-02 are presented for comparison.

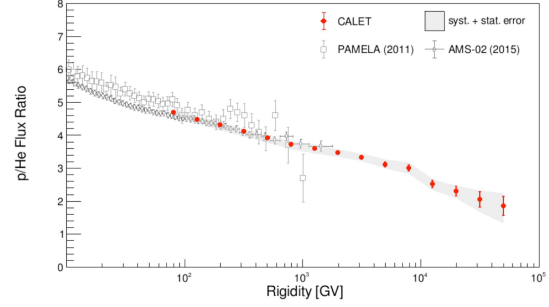


Figure 12: p/He ratio as measured by CALET as a function of rigidity. The red vertical bars represent statistical error only [25]. Measurements from AMS-02 and PAMELA are shown as reference.

and systematic errors, are represented by a yellow band. The main contribution of systematic errors comes from the different MC simulations (EPICS vs. Geant4) used in the analysis, which produce similar selection efficiencies but energy response matrices that differ significantly in the low- and high-energy regions. The resulting fluxes for B (C, O) show discrepancies not exceeding 6 % (10%, 4.5%) below 20 GeV/n and 12% (10%, 12%) above 300 GeV/n, respectively.

In Fig. 13, the energy spectra of B, C and O with CALET are shown and compared with earlier results from space-based [10, 36–41] and balloon-borne [42–45] experiments. The B spectrum is consistent with that of PAMELA [38] and most of the earlier experiments but the absolute normalization is in tension with that of AMS-02, as already pointed out by our previous measurements of the C, O and Fe fluxes [33, 46]. However, we notice that the B/C and B/O ratios are consistent with the ones measured by AMS-02. The C and O spectra shown here are based on a larger dataset but they are consistent with our earlier result [33, 34], and include an improved assessment of systematic errors.

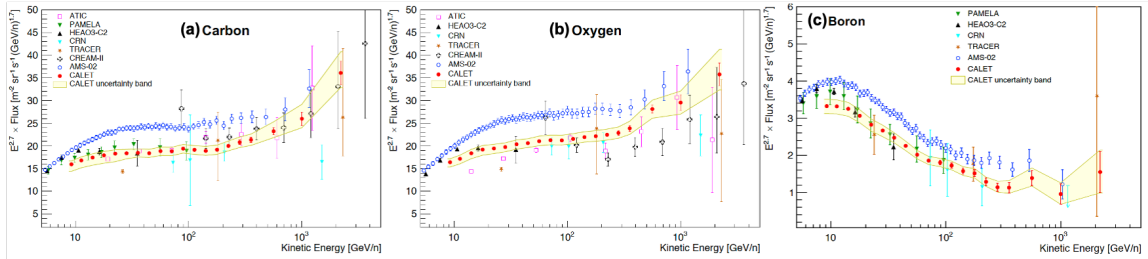


Figure 13: CALET (a) carbon, (b) oxygen, and (c) boron flux (multiplied by $E^{2.7}$). Error bars of CALET data (red) represent the statistical uncertainty only, while the yellow band indicates the quadratic sum of statistical and systematic errors. Also plotted are other direct measurements

Fig. 14 shows the fits to CALET carbon and oxygen data (blue solid line) with a Double Power-Law (DPL) function:

$$\Phi(E) = \begin{cases} C \left(\frac{E}{\text{GeV}}\right)^\gamma & E \leq E_0 \\ C \left(\frac{E}{\text{GeV}}\right)^\gamma \left(\frac{E}{E_0}\right)^{\Delta\gamma} & E > E_0 \end{cases} \quad (2)$$

where C is a normalization factor, γ is the spectral index, and $\Delta\gamma$ is the spectral index change above the transition energy E_0 . A single power-law (SPL) function (Eq. 2 with $\Delta\gamma=0$), fitted to the data

in the energy range of 25 GeV/n to 200 GeV/n and extrapolated above 200 GeV/n, is also shown for comparison (dashed line).

The simultaneous DPL fit to the C and O spectra (with common parameters, except normalization) in the energy range [25, 3800] GeV/n yields $\gamma_{CO} = -2.66 \pm 0.02$, $\Delta\gamma_{CO} = 0.19 \pm 0.04$ and $E_0 = 260 \pm 50$ GeV/n confirming our first results reported in Ref. [33]. Fitting the B flux with fixed E_0 yields $\gamma_B = -3.03 \pm 0.03$, $\Delta\gamma_B = 0.32 \pm 0.14$ with $\chi^2/\text{d.o.f.} = 5.2/11$. The energy spectra are clearly different as expected for primary and secondary CR, and the fit results seem to indicate, albeit with low statistical significance, that the flux hardens more for B than for C and O above 200 GeV/n. A similar indication also comes from the simultaneous fit to the B/C and B/O flux ratios (Fig. 15). Fitting with SPL functions in the energy range [25, 3800] GeV/n yields a mean spectral index $\Gamma = -0.376 \pm 0.014$ ($\chi^2/\text{d.o.f.} = 19/27$). However, a DPL function provides a better fit suggesting a trend of the data towards a flattening of the B/C and B/O ratios at high energy, with a spectral index change $\Delta\Gamma = -0.22 \pm 0.10$ ($\chi^2/\text{d.o.f.} = 15/26$) above E_0 , which is left as a fixed parameter in the fit. This result is consistent with that of AMS-02, and supports the hypothesis that secondary B exhibits a stronger hardening than primaries C and O, although no definitive conclusion can be drawn due to the large uncertainty in $\Delta\Gamma$ given by our present statistics. For the Leaky Box Model fit, the fit with a residual material around SNR of ~ 1 g/cm² gives a better fit than zero material (see Ref. [34] for details).

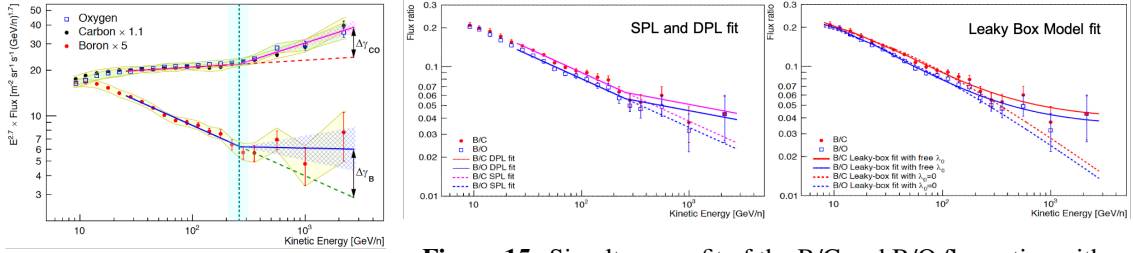


Figure 14: The B, C and O energy spectra are fitted with DPL and SPL function (see text for fitting results).

Figure 15: Simultaneous fit of the B/C and B/O flux ratios with: (Right) SPL (dashed lines) and DPL (solid lines) functions; (Left) a leaky-box model leaving the λ_0 parameter free to vary (solid line) or fixing it at zero (dashed line), respectively.

Iron and Nickel Figure 16(a) shows the preliminary iron spectrum in kinetic energy per nucleon measured by CALET in the energy range from 10 GeV/n to 1000 GeV/n [47]. In this case, the statistics are increased by a factor of 2 compared to the previous publication [46]. The iron spectrum obtained by EPICS is consistent with the spectrum by GEANT4 above 100 GeV/n, while differ in normalization in the low energy region about 10%. This difference can be attributed to the response matrices, which differ significantly in the low-energy region. In this conference, a preliminary result of the iron spectrum below 10 GeV/n was also reported by using an analysis of the geomagnetic effects [48]. Figure 16(b) shows the nickel spectrum in kinetic energy per nucleon measured by CALET in the energy range from 8.8 GeV/n to 240 GeV/n [47]. Here, the statistics are increased by a factor of 1.3 compared to the previous publication [49].

Figure 17(a) shows the fit to the Fe flux with a double power-law (DPL) function (Eq. 2). A single power-law function (SPL) is also shown for comparison. The DPL fit, performed from 50 GeV/n to 1000 GeV/n, gives a $\gamma = -2.60 \pm 0.01(\text{stat}) \pm 0.08(\text{sys})$, $\Delta\gamma = 0.29 \pm 0.27$ and $E_0 = (428 \pm 314)$ GeV/n with $\chi^2/\text{d.o.f.} = 0.82/3$. The SPL fit in the same energy range gives $\gamma = -2.56 \pm 0.01(\text{stat}) \pm 0.03(\text{sys})$, with $\chi^2/\text{d.o.f.} = 2.7/5$. The significance of the fit with the DPL in the studied energy range is not sufficient to exclude the possibility of a single power law. Figure 17(b) shows the fit to the Ni flux with a SPL function performed from 20 GeV/n to 240 GeV/n. The fit result gives $\gamma = -2.49 \pm 0.03(\text{stat}) \pm 0.07(\text{sys})$, with $\chi^2/\text{d.o.f.} = 0.1/3$. This result shows that the Ni flux, in the fit region, is compatible within the errors with a single power law.

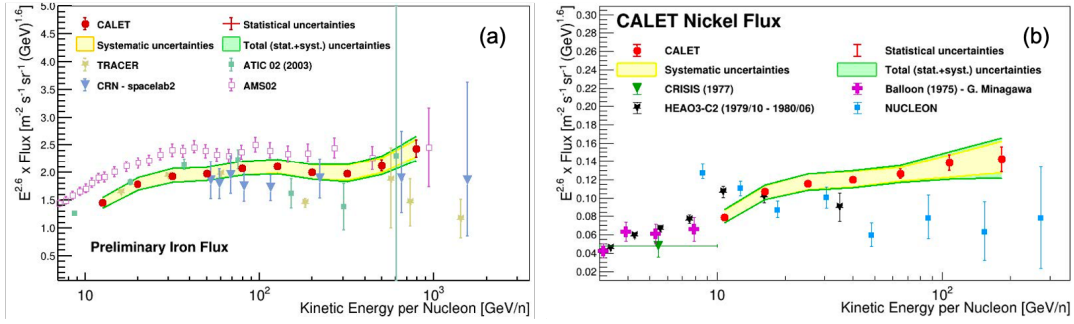


Figure 16: CALET iron (a) and nickel (b) fluxes (multiplied by $E^{2.6}$) as a function of kinetic energy per nucleon. Error bars of the CALET data (red) represent the statistical uncertainty only, the yellow band indicates the quadrature sum of systematic errors, while the green band indicates the quadrature sum of statistical and systematic errors. Also plotted are other direct measurements.

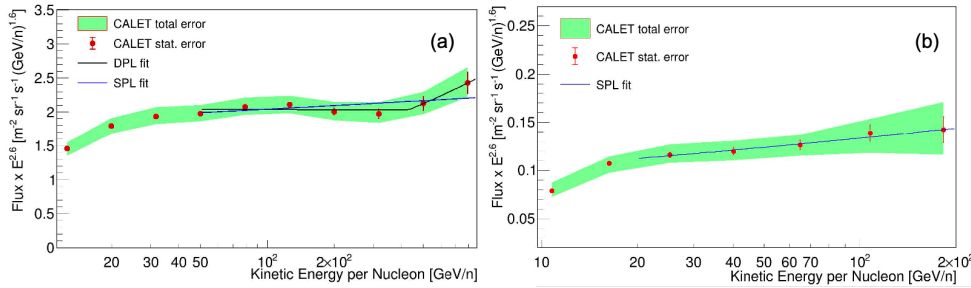


Figure 17: (a) Fit of the CALET iron energy spectrum to an SPL function (blue line) and to a DPL function (black line) in the energy range 50 GeV/n to 1000 GeV/n. (b) Fit of the CALET nickel energy spectrum to an SPL function (blue line). The fluxes are multiplied by $E^{2.6}$ where E is the kinetic energy per nucleon. The error bars are representative of purely statistical errors.

Flux Ratio of Primary Elements With the available data from CALET observations during more than 7 years, it was possible to compute the flux ratio of heavy elements (Fe and Ni) and light ones (He, C, O) and compare them with the ratio of light elements (O/He, C/He and O/C) [50]. As shown in Fig. 18, it emerges that all the ratios are compatible with a constant value above 100 GeV/n (Ni/Fe is constant starting from 10 GeV/n) whereas at low energy the ratio increases in a similar way for Ni/O, Ni/C, Ni/He, Fe/O, Fe/C, Fe/He. The increment at low energy is less pronounced for O/C, O/He and C/He.

Ultra-Heavy Cosmic Rays The measurement of ultra-heavy Galactic cosmic rays (UHGR), ^{30}Zn and higher charge elements, provides insight into the origins of cosmic rays. CALET's measurements of cosmic-ray abundances in the $13 \leq Z \leq 44$ charge range provide complementary measurements and a check of the cross calibrations of other instruments. As reported in Ref. [51], the UH trigger requires events only pass through the CHD and top half of the IMC. This corresponds to an acceptance angle of 75° , which gives an enhanced geometry factor of $4400 \text{ cm}^2 \text{ sr}$ (almost $4 \times$ the total acceptance with the HE trigger). In this trigger, one needs to use the minimum geomagnetic cutoff as a proxy for energy. Here we explore usage of a subset of UH trigger data that requires particles to pass through part of the TASC (~ 65 million events). The results of this fit of charge distribution after the dedicated corrections in the UH region for the data set [52, 53] obtained during 7.5 years of operations, are shown in Fig. 19.

After performing a careful fitting [52], we are able to plot the relative abundances in Fig. 20,

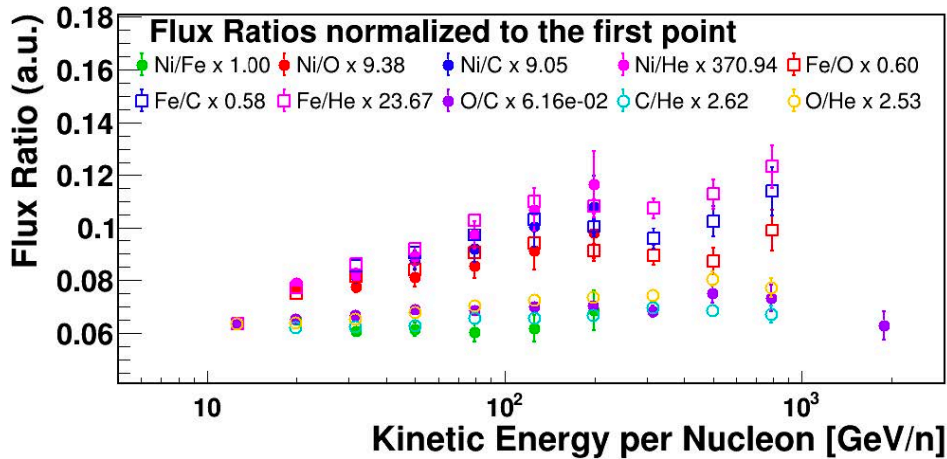


Figure 18: Comparison of CALET flux ratios: Ni/O (red points), Ni/C (blue points), Ni/He (magenta points), Fe/O (red squares), Fe/C (blue squares), Fe/He (magenta squares), O/C (violet points), C/He (cyan points) and O/He (yellow points) are normalized to the first point of Ni/Fe (green points).

in which the results of previous experiments (ACE-CRIS [54] and SuperTIGER.) are compared. For SuperTIGER both the published top-of-instrument values [55] and a set of preliminary top-of-atmosphere values [56] are shown. We also provide a comparison to the older analysis method most recently shown in Ref. [51] that uses the UH trigger in conjunction with a geomagnetic cutoff screen. In these plots, we can see good consistency between the space-based measurements and CALET. We note that there are some minor differences from SuperTIGER, but these may be caused by problems with the atmospheric corrections.

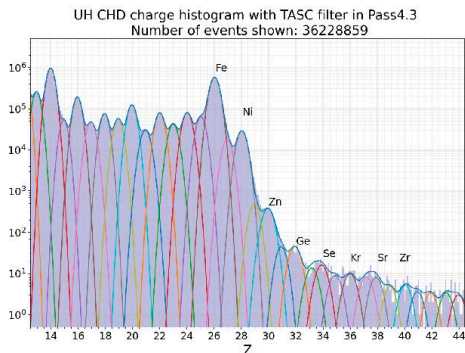


Figure 19: The multigaussian fit for the TASC UH abundances. The number of events within the full fit is roughly identical to the number in the histogram (< 1% difference between fit and histogram in the UH region)

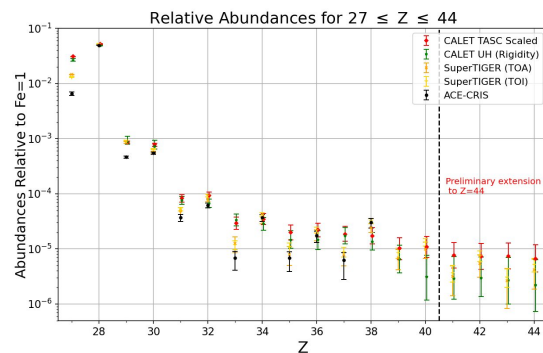


Figure 20: CALET UH Abundances for $Z > 26$ compared to the abundances from ACE-CRIS and both SuperTIGER top of instrument (TOI) and top of atmosphere (TOA). The CALET UH abundances derived via a rigidity cutoff is in red.

4.4 High-Energy Gamma-rays and Gamma-ray Bursts

High-Energy Gamma-rays CALET is sensitive to gamma rays from 1 GeV up to 10 TeV, with the energy resolution and the angular resolution for gamma rays estimated as 3% and 0.4° , respectively, at 10 GeV [57]. Access to energies below 10 GeV is enabled by a dedicated low-energy gamma (LE- γ) trigger which is active only at low geomagnetic latitudes. The highest gamma-ray efficiency is achieved around 10 GeV with an efficiency of 50% relative to a geometrical factor of about $400 \text{ cm}^2 \text{ sr}$, by applying event selections. The gamma-ray events collected during 2637 days of operations with this trigger were presented at this conference [58]. The contribution

of secondary photon background from cosmic-ray interactions with ISS structures in the CALET field-of-view was also reported [59]. Figure 21 shows a sky map of gamma-ray intensities for LE- γ triggers (> 1 GeV). Note that the CAL exposures, superimposed as contours, are not uniform over the celestial coordinates because of the inclination angle (51.6°) of the ISS orbit and our triggering schemes. One can see this sky map matches nicely with those shown by Fermi-LAT, considering the non-uniform exposures. We can easily identify 23 bright point sources in the skymap, but the significance level of the detection of each source is still under evaluation. Without removing point sources, the Galactic plane (diffuse plus discrete sources) spectrum ($|b| < 8^\circ$) and the off-Galactic plane spectrum ($|b| > 10^\circ$) are obtained in 1–100 GeV by LE- γ and in 10–1000 GeV by HE trigger. A good match is seen with the Fermi-LAT results for the Galactic plane spectrum, but some overestimates below about 10 GeV and underestimates above that energy can be seen in the off-plane spectrum [58]. In order to increase the geometrical factor at high energies, we have implemented a refinement of the photon event selection, focusing on the efficiency at energies above 10 GeV. As a result, the increases over the existing selection at 200 GeV and 1 TeV are $\sim 35\%$ and $\sim 200\%$, respectively, for nearly-normal-incidence photons [60].

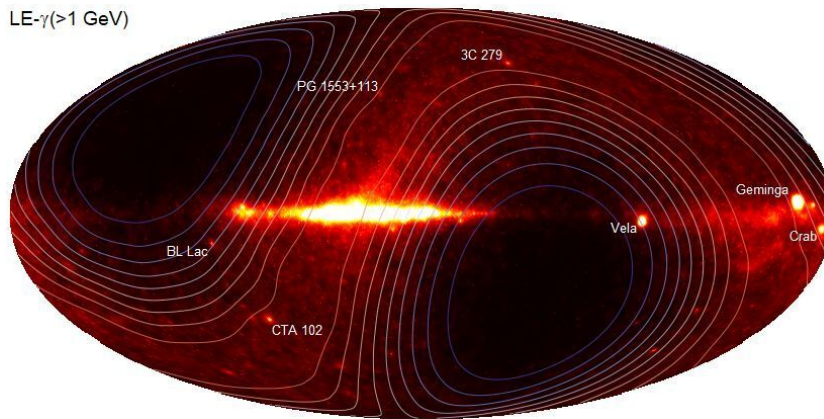


Figure 21: Sky map for LE- γ triggers (> 1 GeV) showing gamma-ray intensities observed in galactic coordinates. Superimposed contours show relative exposures. Only the very bright sources are indicated.

Gamma-rays Bursts The CALET gamma-ray burst monitor (CGBM), designed to observe prompt emissions of gamma-ray bursts (GRBs) in the hard X-ray (7–1000 keV) and soft gamma-ray (40 keV–20 MeV) band, has been providing all-sky monitoring, with 60% duty cycle and without any problems, since October 2015. The gamma-ray bursts are monitored also by the Calorimeter, whose threshold is decreased to 1 GeV whenever a trigger signal is produced by the CGBM. Therefore, CALET covers the energies from 7 keV to 10 TeV with a break between 20 MeV–1 GeV. In Fig. 22, specifications of the CGBM are presented. As of the end of June 2023, the CGBM has detected 327 GRBs, including 31 short GRBs [61]. Figure 23 presents the time duration distribution of GRBs observed by CGBM.

CALET has actively participated in the follow-up campaign for the search of electromagnetic counterparts of the gravitational wave events observed by LIGO/Virgo. Although no candidates have been found, upper limits on the high-energy gamma-ray flux were derived for 20 out of 57 events from the LIGO/Virgo third observation (O3) run [62]. CALET has been searching for electromagnetic counterparts in O4 as well as O3. We have improved analysis pipelines looking toward the search for signals associated with the much-increased rate of gravitational wave events in O4. Once a GCN/LVC NOTICE is distributed via GCN Kafka and the analysis server receives the notice for each event, notice information, including the event name, event time, URL to the sky map FITS data, etc., are stored as a text file in the analysis server. If any text files and high-level

data are available, two pipelines for CGBM and CALorimeter analysis process the high-level data for the quick-look analysis. Also, quick-look analyses are uploaded to the internal web server to check results easily and quickly by collaborators. Although the analysis pipeline checks the GCN/LVC NOTICE every 15 minutes, observation data are distributed hourly, and processing high-level data takes several hours. Therefore, the quick-look analysis takes at least several hours once the GCN/LVC NOTICE is distributed. Although 169 gravitational events have been reported via the GCN/LVC NOTICE and analyzed by the pipelines, only 15 significant events were reported, and the upper limits of 8 events were obtained with the CGBM and CALorimeter search.

	HXM	SGM
Crystal	LaBr ₃ (Ce)	BGO
Number of detectors	2	1
Diameter [mm]	66.1 (small) 78.7 (large)	102
Thickness [mm]	12.7	76
Energy range [keV]	7-1000	40-20000
Field of view	~3 sr	~8 sr

Figure 22: CGBM specifications.

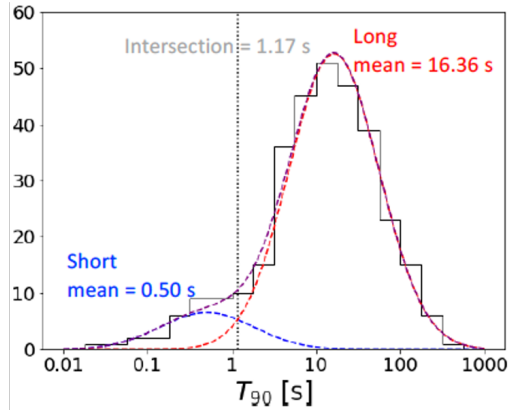


Figure 23: Duration distribution measured by SGM (40–1000 keV).

5. Solar Modulation

CALET observations of low-energy CRs have been successfully performed with a Low-Energy Electron (LEE) shower trigger mode activated only at high geomagnetic latitudes. An analysis of electrons and protons to investigate the solar modulation during the descending phase of the solar cycle 24 was published in Ref. [63], and the extended analysis to the ascending phase of the 25th solar cycle was reported in this conference [64]. We analyzed about 1.03 million electron and 1.71 million proton candidates collected in a total observational live time of about 268 and 269 hours, respectively.

In Fig. 24, the observed variations of electron and proton count rates at an identical average rigidity of 3.8 GV are presented. These variations show a clear charge-sign dependence of the solar modulation of galactic cosmic rays (GCRs), which is consistent with the prediction of a numerical drift model of the GCR transport in the heliosphere described in Ref. [63]. It is also found that the ratio of 3.8 GV proton count rate to the neutron monitor count rate in the ascending phase of solar cycle 25 is clearly different from that in the descending phase of cycle 24. Correlations between the electron (proton) count rate and the heliospheric environmental parameters, such as the current sheet tilt angle, are a useful tool in further developing a numerical model of solar modulation.

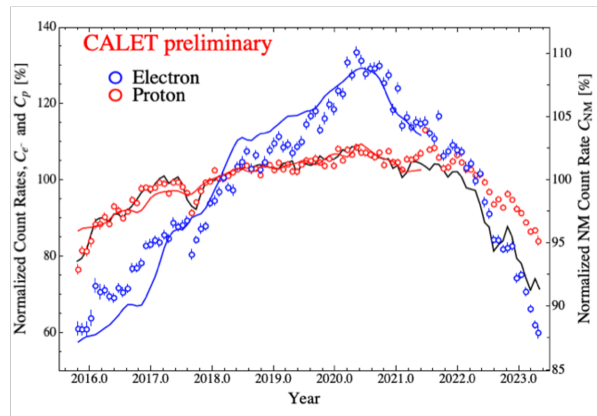


Figure 24: Time profiles of the normalized count rates of electrons C_{e^-} (blue open circles) and protons C_p (red open circles) for each Carrington rotation (left vertical axis), compared with the count rate of a neutron monitor at the Oulu station (black curve) on the right vertical axis and the electron (blue curve) and proton (red curve) count rates reproduced by the numerical drift model.

6. Space Weather

CALET provides a continuous monitoring of space-weather phenomena affecting the near-Earth environment, including solar energetic particle and relativistic electron precipitation (REP) events [65–67]. In the work presented at this conference [68], a method for the detection and categorization of MeV REP events was presented using the dataset obtained in a period from October 2015 to October 2021.

From this catalog we identify a subset of a few hundred REP events observed at times where CALET is in magnetic conjunction with the Van Allen probes. These conjugate measurements enable studies of associated plasma wave data from RBSP-A/B and potential drivers for MeV electron precipitation. An image of the conjugate measurements is illustrated in Fig. 25. We show that roughly 10 percent of the observed REP events are associated with enhanced electromagnetic ion cyclotron (EMIC) wave activity, suggesting that waves can play a significant role in driving MeV electron precipitation.

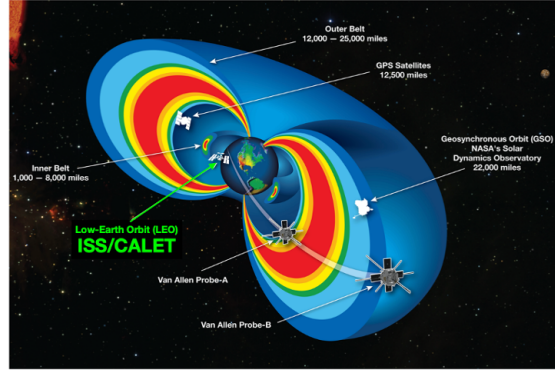


Figure 25: An image view of CALET and Radiation Belt Science Probes (RBSP) on their orbit.

7. Summary and Future Prospects

CALET instrument performance on the ISS has been very stable during the whole scientific observation period from Oct. 13, 2015. At this conference, CALET presented new data based on about 7.5 years of observation and 4.05 billion triggers (for energies > 1 GeV). They include an updated measurement of the electron and positron spectrum up to 7.5 TeV for searches of nearby sources and DM, an update of the proton spectrum to 60 TeV, and a result of the helium spectrum to 250 TeV. Cosmic-ray carbon and oxygen and their flux ratio were also updated up to 3.8 TeV/ n . The spectrum of cosmic-ray iron was revised by using the dataset increased by a factor of two since the last publication up to 1 TeV/ n and the nickel spectrum was updated. The ratios of primary components are investigated to find the effects of secondary particles produced in the propagation process through the Galaxy. Improved analyses of CALET UHCR were also presented, as well as gamma-ray measurements, GRB observations and searches of GW event counterparts. The charge-dependent solar modulation was clearly observed during the descending phase of the solar cycle 24, and the observation is extended to the 25th cycle. The REP observations related to space weather are succeeded to identify the origin of REP.

Extended CALET operations were approved by JAXA/NASA/ASI in March 2021 through the end of 2024, and a further extension to 2030 is expected. Improved statistics and refinement of the analyses with additional data collected during the live time of the mission will allow to extend the measurements to higher energies and improve the spectral analyses, contributing to a better understanding of CR phenomena.

Acknowledgements

We gratefully acknowledge JAXA's contributions to the development of CALET and to the operations onboard the International Space Station. The CALET effort in Italy is supported by ASI under Agreement No.2013-018-R.0 and its amendments. The CALET effort in the United States is supported by NASA through Grants No. 80NSSC20K0397, No. 80NSSC20K0399, and NNH18ZDA001N-APRA18-0004. This work is supported by JSPS KAKENHI Grant Numbers 19H05608 and 21K03592 in Japan.

References

- [1] O. Adriani *et al.* (CALET Collaboration), Phys. Rev. Lett. **119** 181101 (2017).
- [2] Y. Asaoka, Y. Akaike *et al.* (CALET Collaboration), Astropart. Phys. **91** 1 (2017).
- [3] Y. Asaoka, S. Ozawa, S. Torii *et al.* (CALET Collaboration), Astropart. Phys. **100** 29 (2018).
- [4] T. Tamura, Y. Akaike and K. Kobayashi (for the CALET Collaboration), in *PoS (ICRC2023)* 94 (2023).
- [5] Y. Akaike and S. Torii (CALET Collaboration), in *PoS (ICRC2023)* 71 (2023).
- [6] O. Adriani *et al.* (CALET Collaboration), Phys. Rev. Lett. *to be published*.
- [7] O. Adriani *et al.* (CALET Collaboration), Phys. Rev. Lett. **120** 261102 (2018).
- [8] S. Gonzi, L. Pacini and E. Berti (for the CALET Collaboration), in *PoS (ICRC2023)* 90 (2023).
- [9] S. Abdollahi *et al.* (Fermi-LAT Collaboration), Phys. Rev. D **95** 082007 (2017).
- [10] M. Aguilar *et al.* (AMS-02 Collaboration), Phys. Rep. **894** 1 (2021).
- [11] G. Ambrosi *et al.* (DAMPE Collaboration), Nature **552**, 63 (2017).
- [12] J. Nishimura *et al.*, Astrophys. J. **238**, 394 (1980).
- [13] T. Kobayashi *et al.*, Astrophys. J. **601**, 340 (2004).
- [14] S. Torii and Y. Akaike (for the CALET Collaboration), in *PoS(ICRC2021)* 105 (2021).
- [15] M. Aguilar *et al.* (AMS-02 Collaboration), Phys. Rev. Lett. **122**, 041102 (2019).
- [16] H. Motz (for the CALET Collaboration), in *PoS (ICRC2023)* 67 (2023).
- [17] N. Cannaday, Y. Akaike and S. Torii (for the CALET Collaboration), in *PoS (ICRC2023)* 62 (2023).
- [18] H. Motz (for the CALET Collaboration), in *PoS (ICRC2023)* 1385 (2023).
- [19] K. Kobayashi and P.S. Marrocchesi (for the CALET Collaboration), in *PoS (ICRC2023)* 92 (2023).
- [20] O. Adriani *et al.* (CALET Collaboration), Phys. Rev. Lett. **122** 181102 (2019).
- [21] O. Adriani *et al.* (CALET Collaboration), Phys. Rev. Lett. **129** 101102 (2022).
- [22] M. Aguilar *et al.* (AMS-02 Collaboration), Phys. Rev. Lett. **114**, 171103 (2015).
- [23] Y.S. Yoon *et al.* (CREAM-III Collaboration), Astrophys. J. **839**, 5 (2017).
- [24] Q. An *et al.* (DAMPE Collaboration), Sci. Adv. **5(9)**, eaax3793 (2019).
- [25] O. Adriani *et al.* (CALET Collaboration), Phys. Rev. Lett. **130** 171002 (2023).
- [26] P. Brogi and K. Kobayashi (for the CALET Collaboration), in *PoS (ICRC2023)* 54 (2023).
- [27] F. Alemanno *et al.* (DAMPE Collaboration), Phys. Rev. Lett. **126**, 201102 (2021).
- [28] M. Aguilar *et al.* (AMS-02 Collaboration), Phys. Rev. Lett. **115**, 211101 (2015).
- [29] Y. S. Yoon *et al.*, Astrophys. J. **839**, 5 (2017).
- [30] M. Mattiazzi and P. Brogi (for the CALET Collaboration), in *PoS (ICRC2023)* 82 (2023).
- [31] M. Aguilar *et al.* (AMS Collaboration), Phys. Rev. Lett. **123**, 181102 (2019).
- [32] O. Adriani *et al.* (PAMELA Collaboration), Science **332**, 69 (2011).
- [33] O. Adriani *et al.* (CALET Collaboration), Phys. Rev. Lett. **125** 251102 (2020).
- [34] O. Adriani *et al.* (CALET Collaboration), Phys. Rev. Lett. **129** 251103 (2022).
- [35] P. Maestro and Y. Akaike (for the CALET Collaboration), in *PoS (ICRC2023)* 58 (2023).
- [36] J. J. Engelmann *et al.* (HEAO-3), Astron. Astrophys. **233**, 96 (1990).

- [37] S.P. Swordy *et al.* (CRN), *Astrophys. J.* **349**, 625 (1990).
- [38] O. Adriani *et al.* (PAMELA), *Astrophys. J.* **93**, 791 (2014).
- [39] M. Aguilar *et al.* (AMS), *Phys. Rev. Lett.* **117**, 231102 (2016).
- [40] M. Aguilar *et al.* (AMS), *Phys. Rev. Lett.* **120**, 021101 (2018).
- [41] F. Alemanno *et al.* (DAMPE), *Science Bulletin* **67**, 2162 (2022).
- [42] H. S. Ahn *et al.* (CREAM), *Astroparticle Phys.* **30**, 133 (2008).
- [43] A. Obermeier *et al.* (TRACER), *Astrophys. J.* **752**, 69 (2012).
- [44] A. Panov *et al.* (ATIC), *Bull. Russian Acad. Sci.* **73**, 564 (2009).
- [45] H. S. Ahn *et al.* (CREAM), *Astrophys. J.* **707**, 593 (2009).
- [46] O. Adriani *et al.* (CALET Collaboration), *Phys. Rev. Lett.* **126** 241101 (2021).
- [47] F. Stolzi, Y. Akaike, G. Bigongiari and C. Checchia (for the CALET Collaboration), in *PoS (ICRC2023)* 61 (2023).
- [48] M. Ichimura and K. Kasahara (for the CALET Collaboration), in *PoS (ICRC2023)* 57 (2023).
- [49] O. Adriani *et al.* (CALET Collaboration), *Phys. Rev. Lett.* **128** 131103 (2022).
- [50] C. Checchia, Y. Akaike and F. Stolzi (for the CALET Collaboration), in *PoS (ICRC2023)* 93 (2023).
- [51] W.V. Zober *et al.* (for the CALET Collaboration), in *PoS(ICRC2021)* 124 (2021).
- [52] W. Zober and B. Rauch (for the CALET Collaboration), in *PoS (ICRC2023)* 88 (2023).
- [53] W. Zober and B. Rauch (for the CALET Collaboration), in *PoS (ICRC2023)* 89 (2023).
- [54] W.R. Binns *et al.*, *Astrophys. J.* **936**, 13 (2022).
- [55] N. Walsh *et al.*, *Advances in Space Research*, **70**, 2666 (2022).
- [56] N. Walsh, Doctoral dissertation, Washington University in St. Louis (2020).
- [57] N. Cannady *et al.* (CALET Collaboration), *Astrophys. J. Suppl.* **238**, 5 (2018).
- [58] M. Mori and N. Cannaday (for the CALET Collaboration), in *PoS (ICRC2023)* 708 (2023).
- [59] N. Cannaday and Y. Kawakubo (for the CALET Collaboration), in *PoS (ICRC2023)* 63 (2023).
- [60] N. Cannaday (for the CALET Collaboration), in *PoS (ICRC2023)* 657 (2023).
- [61] Y. Kawakubo, M. Cherry and T. Sakamoto (for the CALET Collaboration), in *PoS (ICRC2023)* 1517 (2023).
- [62] O. Adriani *et al.* (CALET Collaboration) *Astrophys. J.* **933:85** (2022).
- [63] O. Adriani *et al.* (CALET Collaboration), *Phys. Rev. Lett.* **130** 211001 (2023).
- [64] S. Miyake, K. Munakata and Y. Akaike (for the CALET Collaboration), in *PoS (ICRC2023)* 1253 (2023).
- [65] R. Kataoka *et al.*, *Geophys. Res. Lett.*, **43** 10.1002/2016GL068930 (2016).
- [66] R. Kataoka *et al.*, *Journal of Geophysical Research: Space Physics* **125** e2020JA027875 (2020).
- [67] A. Bruno *et al.*, *Geophysical Research Letters*, **49** e2021GL097529 (2022).
- [68] A. Ficklin, A. Bruno, L. Blum, G. de Nolfo T. Gregory Guzik, R. Kataoka and S. Vidal-Lueng (for the CALET Collaboration), in *PoS (ICRC2023)* 176 (2023).

Full Author List: CALET Collaboration

O. Adriani^{1,2}, Y. Akaike^{3,4}, K. Asano⁵, Y. Asaoka⁵, E. Berti^{2,6}, G. Bigongiari^{7,8}, W.R. Binns⁹, M. Bongi^{1,2}, P. Brogi^{7,8}, A. Bruno¹⁰, N. Cannady^{11,12,13}, G. Castellini⁶, C. Checchia^{7,8}, M.L. Cherry¹⁴, G. Collazuol^{15,16}, G.A. de Nolfo¹⁰, K. Ebisawa¹⁷, A.W. Ficklin¹⁴, H. Fuke¹⁷, S. Gonzi^{1,2,6}, T.G. Guzik¹⁴, T. Hams¹¹, K. Hibino¹⁸, M. Ichimura¹⁹, K. Ioka²⁰, W. Ishizaki⁵, M.H. Israel⁹, K. Kasahara²¹, J. Kataoka²², R. Kataoka²³, Y. Katayose²⁴, C. Kato²⁵, N. Kawanaka²⁰, Y. Kawakubo¹⁴, K. Kobayashi^{3,4}, K. Kohri²⁶, H.S. Krawczynski⁹, J.F. Krizmanic¹², P. Maestro^{7,8}, P.S. Marrocchesi^{7,8}, A.M. Messineo^{8,27}, J.W. Mitchell¹², S. Miyake²⁸, A.A. Moiseev^{29,12,13}, M. Mori³⁰, N. Mori², H.M. Motz¹⁸, K. Munakata²⁵, S. Nakahira¹⁷, J. Nishimura¹⁷, S. Okuno¹⁸, J.F. Ormes³¹, S. Ozawa³², L. Pacini^{2,6}, P. Papini², B.F. Rauch⁹, S.B. Ricciarini^{2,6}, K. Sakai^{11,12,13}, T. Sakamoto³³, M. Sasaki^{29,12,13}, Y. Shimizu¹⁸, A. Shiomi³⁴, P. Spillantini¹, F. Stolzi^{7,8}, S. Sugita³³, A. Sulaj^{7,8}, M. Takita⁵, T. Tamura¹⁸, T. Terasawa⁵, S. Torii³, Y. Tsunesada^{35,36}, Y. Uchihori³⁷, E. Vannuccini², J.P. Wefel¹⁴, K. Yamaoka³⁸, S. Yanagita³⁹, A. Yoshida³³, K. Yoshida²¹, and W.V. Zober⁹

¹Department of Physics, University of Florence, Via Sansone, 1 - 50019, Sesto Fiorentino, Italy, ²INFN Sezione di Firenze, Via Sansone, 1 - 50019, Sesto Fiorentino, Italy, ³Waseda Research Institute for Science and Engineering, Waseda University, 17 Kikuicho, Shinjuku, Tokyo 162-0044, Japan, ⁴JEM Utilization Center, Human Spaceflight Technology Directorate, Japan Aerospace Exploration Agency, 2-1-1 Sengen, Tsukuba, Ibaraki 305-8505, Japan, ⁵Institute for Cosmic Ray Research, The University of Tokyo, 5-1-5 Kashiwa-no-Ha, Kashiwa, Chiba 277-8582, Japan, ⁶Institute of Applied Physics (IFAC), National Research Council (CNR), Via Madonna del Piano, 10, 50019, Sesto Fiorentino, Italy, ⁷Department of Physical Sciences, Earth and Environment, University of Siena, via Roma 56, 53100 Siena, Italy, ⁸INFN Sezione di Pisa, Polo Fibonacci, Largo B. Pontecorvo, 3 - 56127 Pisa, Italy, ⁹Department of Physics and McDonnell Center for the Space Sciences, Washington University, One Brookings Drive, St. Louis, Missouri 63130-4899, USA, ¹⁰Heliospheric Physics Laboratory, NASA/GSFC, Greenbelt, Maryland 20771, USA, ¹¹Center for Space Sciences and Technology, University of Maryland, Baltimore County, 1000 Hilltop Circle, Baltimore, Maryland 21250, USA, ¹²Astroparticle Physics Laboratory, NASA/GSFC, Greenbelt, Maryland 20771, USA, ¹³Center for Research and Exploration in Space Sciences and Technology, NASA/GSFC, Greenbelt, Maryland 20771, USA, ¹⁴Department of Physics and Astronomy, Louisiana State University, 202 Nicholson Hall, Baton Rouge, Louisiana 70803, USA, ¹⁵Department of Physics and Astronomy, University of Padova, Via Marzolo, 8, 35131 Padova, Italy, ¹⁶INFN Sezione di Padova, Via Marzolo, 8, 35131 Padova, Italy, ¹⁷Institute of Space and Astronautical Science, Japan Aerospace Exploration Agency, 3-1-1 Yoshinodai, Chuo, Sagamihara, Kanagawa 252-5210, Japan, ¹⁸Kanagawa University, 3-27-1 Rokkakubashi, Kanagawa, Yokohama, Kanagawa 221-8686, Japan, ¹⁹Faculty of Science and Technology, Graduate School of Science and Technology, Hirosaki University, 3, Bunkyo, Hirosaki, Aomori 036-8561, Japan, ²⁰Yukawa Institute for Theoretical Physics, Kyoto University, Kitashirakawa Oiwake-cho, Sakyo-ku, Kyoto, 606-8502, Japan, ²¹Department of Electronic Information Systems, Shibaura Institute of Technology, 307 Fukasaku, Minuma, Saitama 337-8570, Japan, ²²School of Advanced Science and Engineering, Waseda University, 3-4-1 Okubo, Shinjuku, Tokyo 169-8555, Japan, ²³National Institute of Polar Research, 10-3, Midori-cho, Tachikawa, Tokyo 190-8518, Japan, ²⁴Faculty of Engineering, Division of Intelligent Systems Engineering, Yokohama National University, 79-5 Tokiwadai, Hodogaya, Yokohama 240-8501, Japan, ²⁵Faculty of Science, Shinshu University, 3-1-1 Asahi, Matsumoto, Nagano 390-8621, Japan, ²⁶Institute of Particle and Nuclear Studies, High Energy Accelerator Research Organization, 1-1 Oho, Tsukuba, Ibaraki, 305-0801, Japan, ²⁷University of Pisa, Polo Fibonacci, Largo B. Pontecorvo, 3 - 56127 Pisa, Italy, ²⁸Department of Electrical and Electronic Systems Engineering, National Institute of Technology (KOSEN), Ibaraki College, 866 Nakane, Hitachinaka, Ibaraki 312-8508, Japan, ²⁹Department of Astronomy, University of Maryland, College Park, Maryland 20742, USA, ³⁰Department of Physical Sciences, College of Science and Engineering, Ritsumeikan University, Shiga 525-8577, Japan, ³¹Department of Physics and Astronomy, University of Denver, Physics Building, Room 211, 2112 East Wesley Avenue, Denver, Colorado 80208-6900, USA, ³²Quantum ICT Advanced Development Center, National Institute of Information and Communications Technology, 4-2-1 Nukui-Kitamachi, Koganei, Tokyo 184-8795, Japan, ³³College of Science and Engineering, Department of Physics and Mathematics, Aoyama Gakuin University, 5-10-1 Fuchinobe, Chuo, Sagamihara, Kanagawa 252-5258, Japan, ³⁴College of Industrial Technology, Nihon University, 1-2-1 Izumi, Narashino, Chiba 275-8575, Japan, ³⁵Graduate School of Science, Osaka Metropolitan University, Sugimoto, Sumiyoshi, Osaka 558-8585, Japan, ³⁶Nambu Yoichiro Institute for Theoretical and Experimental Physics, Osaka Metropolitan University, Sugimoto, Sumiyoshi, Osaka 558-8585, Japan, ³⁷National Institutes for Quantum and Radiation Science and Technology, 4-9-1 Anagawa, Inage, Chiba 263-8555, Japan, ³⁸Nagoya University, Furo, Chikusa, Nagoya 464-8601, Japan, ³⁹College of Science, Ibaraki University, 2-1-1 Bunkyo, Mito, Ibaraki 310-8512, Japan